Journal of Manufacturing Processes 133 (2025) 479–490

Contents lists available at ScienceDirect

Journal of Manufacturing Processes

journal homepage: www.elsevier.com/locate/manpro

Full length article

X-ray tomography of polarization effects on deep laser-machined microgrooves

Ce Xiao [a], Jean-Yves Buffiere [b,*], Arnaud Weck [c]

[a] School of Mechanical Engineering, Xi'an Jiaotong University, Xi'an, 710049, Shaanxi, China
[b] University of Lyon, INSA Lyon, CNRS, MATEIS UMR5510, Villeurbanne, 69621, Lyon, France
[c] Department of Mechanical Engineering, Faculty of Engineering, University of Ottawa, Ottawa, K1N 6N5, ON, Canada

ARTICLE INFO

Keywords:
Femtosecond laser
Machining
Deep grooves
X-ray tomography
Polarization
Ultrafast laser
3D imaging
High aspect ratio grooves
Branching

ABSTRACT

Ultrafast laser machining has been researched extensively over the last few decades to create features such as holes in a variety of materials. The effects of laser parameters including power and polarization on the dynamics of hole formation and resulting hole geometry have been studied. Grooves formation, especially deep ones, on the other hand, has not attracted as much attention, even though grooves are essential to most laser cutting operations. One aspect limiting the study of deep machined features such as grooves is the difficulty in imaging not only the geometry but also the associated collateral damage produced in the material during machining. Here, we employed x-ray tomography for three-dimensional imaging of deep ultrafast laser-machined grooves in various metals. The 3D images of the deep grooves were quantitatively analyzed, revealing the significant effect of laser polarization on groove morphology. Under rotating polarization (also called "scrambled polarization" or "polarization trepanning"), the deep grooves are smooth and uniform, while under linear polarization, extensive branching is observed along the groove, and becomes more pronounced with increasing laser energy and groove entrance length. A mechanistic picture based on laser light reflection off the groove walls is proposed to qualitatively explain the polarization-dependent groove branching observed experimentally. These findings provide new insights into high-precision deep groove laser machining, highlighting the effectiveness of x-ray tomography as a powerful tool for in-depth three-dimensional studies of laser machining processes.

1. Introduction

Femtosecond laser machining stands as a critical technology for the efficient creation of microscale features via cutting, drilling, and grooving, and can be used in virtually any material [1] including metals [2–5], semiconductors [6,7], polymers [8–10], and ceramics [11–14]. Despite extensive research on the ablation of shallow features and the formation of surface morphologies such as laser-induced periodic surface structures (LIPSS) [15–18], understanding the formation mechanisms of microscale high aspect ratio features remains a significant challenge due to the complex laser–matter interactions involved.

Often, deep holes deviate from their intended linear paths, exhibiting bending or other changes in their shape [19]. Several theories have been proposed to explain the irregular shapes observed in deep micro-hole laser machining. Most results in the literature have been explained by the uneven energy distribution inside the hole, attributed to polarization-dependent reflections off the hole walls [20,21]. Tao et al. [22] pointed out that the primary cause of changes in the laser beam profile within micro-holes is the boundary conditions set by the hole sidewalls. In this context, a hole generated by preceding laser pulses may function as a waveguide, where its sidewalls markedly influence the beam profile of subsequent pulses entering the hole. Jiao et al. [23] proposed a theoretical analysis on the effect of hole taper angle on the laser beam propagation by reflection inside micro-holes. Other theories to explain hole morphology are based on non-linear optical effect such as self-focusing and beam filamentation during the drilling process that can alter the characteristics of the laser machined channel. Shah et al. [24] noted that the presence of ablation residues can result in nonlinear interactions between the laser pulses and the atmosphere within the hole. Initially, drilling above the air ionization threshold does not affect the process adversely. Yet, after a certain depth is reached, a marked change in ablation is observed and correlated to beam filamentation. The bending of deep holes was also ascribed to laser scattering or deflection on ablation residues [25]. Xia et al. [19] discovered in their experiments that reducing the ambient

* Corresponding author.
E-mail addresses: jean-yves.buffiere@insa-lyon.fr (J.-Y. Buffiere), aweck@uottawa.ca (A. Weck).

https://doi.org/10.1016/j.jmapro.2024.11.056
Received 5 June 2024; Received in revised form 28 October 2024; Accepted 21 November 2024
Available online 30 November 2024

pressure made the micro-holes straighter and deeper. They ascertained that interference of the laser beam with dynamically scattered ablation aerosols in milliseconds is the main reason for the bending phenomenon observed in deep holes.

The polarization of the laser also significantly influences hole deviation, playing a crucial role in determining the micro-hole's final morphology [20,26]. Nolte et al. [20] were one of the first to demonstrate how high aspect ratio (depth/diameter) holes machined with a laser in stainless steel foils become elliptical when they exit the material and how hole circularity can be maintained when using rotating polarization (or polarization trepanning). Many subsequent studies have confirmed these observations either using rotating polarization or circularly polarized light. Wang et al. [27], for example used circular polarization to drill circular holes in Inconel 718 superalloy. Similarly, Liu et al. [28] observed that in brass plates, when the hole depth exceeded 200 μm, they no longer maintained a standard circular shape. The application of polarization trepanning resulted in circular holes again.

Although there is considerable research on the mechanisms of morphological changes in deep holes during laser machining, studies on deep, high aspect ratio micro-grooves are relatively scarce. Chen et al. [29] demonstrated the formation of deep grooves in a SiAlCN ceramic using a femtosecond laser, obtaining dimensions of 30 μm in width and 280 μm in depth. Borowiec et al. [30] created micro-groove in indium phosphide, reaching a depth of 100 μm. In a different study, Chen et al. [31] employed a laser-induced thermochemical wet etching process to fabricate high aspect ratio (HAR) micro-grooves in stainless steel, with depths reaching up to 250 μm. Studies on very deep grooves is limited, particularly those exceeding 500 μm in depth while maintaining a narrow opening, which, to our knowledge, has yet to be explored in metals. Grooves machining is a precursor to many cutting operations [32–35] as well as in fundamental studies looking at creating artificial internal defects for studying material fracture [36,37].

To date, X-ray computed tomography (X-CT) is the only non-destructive 3D characterization technique for metals with a resolution close to that of optical microscopy [38,39]. It has been widely applied for the quantitative characterization of internal defects, holes, and micro-cracks inside materials in three dimensions [40–42]. More recently, X-CT has also been employed to study the interaction between lasers and materials during laser processing. For example, Nasrollahi et al. [43] used laboratory X-ray tomography to measure percussion-drilled craters in silicon nitride, while Vanwersch et al. [44] applied a similar technique to analyze femtosecond laser-ablated geometries in low-corrosion tool steel. Compared to laboratory CT, synchrotron X-ray tomography offers superior resolution and visibility of defects due to the added benefit of phase contrast [38,45]. As a result, in this paper, synchrotron tomography was employed to explore the influence of laser parameters on the machining of deep grooves in metals.

This paper focuses on fabricating deep micro-grooves in various structural metallic materials (aluminum, titanium, and cast iron) using an ultrafast laser and characterizing their three-dimensional morphological features using synchrotron radiation x-ray tomography. Through image segmentation and 3D rendering, this study provides a quantitative description of the effect of laser parameters and in particular laser polarization on groove morphology. We propose a mechanistic picture for the observed groove branching under linearly polarized light based on polarization dependent reflections inside the groove.

2. Methods

2.1. Materials

In this study, deep grooves were machined in three different metals: pure aluminum (Al) with a purity of 99.7%, pure titanium (Ti) with a purity of 99.7%, and nodular cast iron. The nodular cast iron studied here, used for car component production, remains untreated post-casting. Its microstructure comprises a ferrite matrix with less than 5% volume fraction of pearlite. The average grain size of ferrite is around 50 μm. The matrix contains graphite nodules, averaging 15 μm in diameter. Further details on the microstructure and mechanical properties of this material can be found in [37].

2.2. Laser machining

Samples were machined at a wavelength of 1030 nm using a Light Conversion PHAROS femtosecond laser, with 320 fs pulses at a repetition rate of 30 kHz and a power of 1 W and 3 W resulting in a pulse energy of 0.03 mJ and 0.1 mJ respectively (as measured using an Ophir VEGA digital multimeter and thermal sensor (Ophir 3A-P-Quad)). As shown in Fig. 1a, the pulse energy was adjusted by rotating the polarization with a half waveplate followed by a Glan-laser calcite polarizer which allows parallel polarization to pass through while perpendicular polarization is rejected into a beam dump. The position of the laser on the samples was controlled using an Aerotech AGV-10HPO galvo scanner mounted on an Aerotech ANT130-L-ZS nano-positioning lift stage with z-axis control. The laser was focused using a telecentric f-Theta lens with a 50 mm focal length resulting in an ablation spot size of approximately 18 μm in diameter. To ensure proper focusing of the laser beam on the sample surface, a calibrated imaging system with a LED white light, optical elements, and a CCD camera was used (see yellow beam paths in Fig. 1a). The laser beam was moved back and forth using one of the galvo scanner axes at a speed of 10 mm/s to create a machined line. To prevent excessive energy deposition in the material during the acceleration and deceleration phases of the galvo scanner, the laser shutter is open only after the acceleration phase and closed before the deceleration phase, ensuring a constant speed during machining. Lines of length 0.1 mm and 0.5 mm were created with varying number of passes (i.e. number of back and forth motions). Both linear and rotating polarizations (also called "scrambled" polarization or polarization "trepanning") are studied as shown in Fig. 1b. Constantly rotating linear polarization is obtained by a motor-driven device (Scorpion HKII-2221-6) rotating a half wave-plate at 3230 rpm, resulting in pulses with random polarization reaching the sample during machining.

2.3. X-ray tomography imaging

After laser machining, the 1 mm thickness sheets containing the grooves were cut into needle shaped specimens compatible with tomographic imaging (length about 20 mm, section 1×1 mm^2). Synchrotron Radiation Computed tomography (SRCT) imaging was performed at the European Synchrotron Radiation Facility (ESRF) in Grenoble (France) on Beamline ID11, using a 192 mm sample-detector distance, 55 keV energy, and a voxel size of 1.3 μm with a 2048 × 2048 low noise sCMOS detector. The classical filtered back projection (FBP) algorithm was utilized for image reconstruction without employing any phase retrieval methods. Because of the large coherence of the synchrotron X-ray beam, FBP reconstruction produces Fresnel fringes at the groove edges (phase contrast), which poses challenges for the accurate measurement of groove dimensions [45]. For verification purposes, one of the Ti samples was imaged using a laboratory tomography system $V|TOME|X$ at MATEIS laboratory (no phase contrast in reconstructed images). Two different voxel sizes, 1.3 μm and 0.7 μm, were employed. The lab-based imaging was carried out with an acceleration voltage of 140 kV and a current of 120 μA to ensure 10% transmission of the X-ray beam through the 1 mm diameter cross-section. Additionally, a 0.3 mm thick copper filter was introduced to mitigate beam hardening effects. The same classical FBP algorithm was applied to reconstruct the projected Lab-CT images, maintaining consistency in the reconstruction approach between SRCT and Lab-CT imaging.

In this paper, a total of 77 grooves fabricated under different laser parameters in the three different materials were imaged using synchrotron tomography with different machining parameters shown in Table 1.

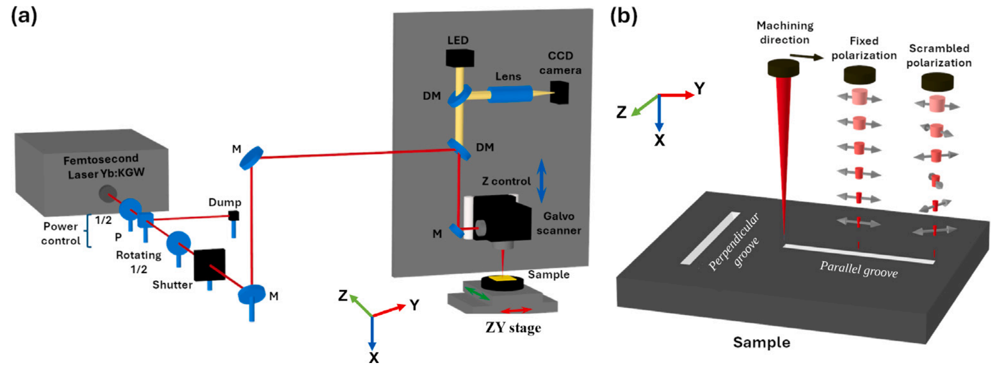

Fig. 1. (a) Schematic of the laser machining experimental setup. 1/2 = half waveplate, P = Glan-laser calcite polarizer, Dump = laser beam dump, Rotating 1/2 = the rotating half waveplate used for creating scrambled polarization, M = mirror, DM = dielectric mirror. (b) Schematic showing the two groove orientations studied here (parallel resulting in s-polarization and perpendicular resulting in p-polarization) as well as the scrambled polarization (also called rotating polarization or polarization trepanning) where pulses reach the sample with a random polarization.

Table 1
Laser processing parameters for the grooves machined in this study.

Material	Polarization	Groove length	Power	Direction	Number of laser passes
Ti	Linear	100 µm	3 W	parallel	5 10 15 20 40 80
Ti	Linear	500 µm	3 W	parallel	5 10 15 20 40 80 160 320
Ti	Scrambled	100 µm	3 W	parallel	5 10 15 20 40 80
Ti	Linear	100 µm	3 W	perpendicular	5 10 15 20 40
Ti	Scrambled	500 µm	3 W	parallel	5 10 15 20 40 80
Ti	Linear	100 µm	1 W	parallel	5 10 15 20 40 80
Ti	Linear	500 µm	1 W	parallel	5 10 15 20 40 80
Cast iron	Linear	100 µm	3 W	parallel	5 10 15 20 40 80
Cast iron	Linear	500 µm	3 W	parallel	40 80
Cast iron	Scrambled	100 µm	3 W	parallel	5 10 15 20 40 80 160 320
Cast iron	Scrambled	500 µm	3 W	parallel	40 80
Al	Linear	500 µm	3 W	parallel	40 80 160 320
Al	Scrambled	100 µm	3 W	parallel	10 20 80 320
Al	Scrambled	500 µm	3 W	parallel	5 10 15 20 40 80 160 320

2.4. 3D rendering and groove dimensions

The three-dimensional gray-level images of the grooves were first segmented. This step is important for visualizing the grooves morphology in 3D and facilitating their quantitative geometrical analysis. In this section, a 3D image of one aluminum sample is taken as an example to illustrate the steps carried out on each groove. Fig. 2a shows four grooves created using linearly polarized laser pulses with a power of 3 W, and 5, 10, 15, and 20 laser passes. The length of the laser machined grooves (taken along the Y axis in Fig. 2) is 500 µm. The grooves were first segmented from the gray level reconstructed images utilizing the Isodata segmentation algorithm, which is the default method in the Fiji software [46]. Subsequently, 3D Erode and Dilate algorithms were applied to mitigate noise. The resulting thresholded binary image and the 3D rendering of the four grooves are exhibited in Fig. 2b and c.

As illustrated in Fig. 2c, the grooves exhibit a relatively flat morphology at the entrance, progressively developing small branches on either side of the main path as the laser penetrates deeper into the material. Groove length maps were generated by integrating the binary image along the groove's length direction (Y-axis in Fig. 2a), with varying colors in Fig. 2d representing the grooves' integral lengths. To achieve a more precise delineation of groove envelopes, the groove length map was further refined by applying a threshold value of 10 µm (Fig. 2e). This thresholding aimed at reducing noise while retaining the finer branches of the groove as much as possible. Fig. 2f depicts the measurement of three key groove feature dimensions: the depth of the groove's envelope (L1), the opening of the groove's envelope (L2), and the depth of the flat portion of the groove (L3).

3. Results

3.1. Effect of laser polarization on groove shape

Fig. 3 illustrates the geometry of deep grooves machined within aluminum (Al), titanium (Ti), and cast iron, using both linear and scrambled polarization while with a laser power of 3 W, an entrance length of (500 µm), and 80 laser passes. Those images have been analyzed following the procedure described in the previous section. In all three materials, a significant divergence or branching occurs in the grooves beyond a depth of 100-200 µm when linear polarization was employed. This branching was characterized by the formation of numerous smaller, inclined channels diverging from the primary channel, with an angle ranging from 30 to 40°. In cast iron, the divergence was more pronounced, with many of these smaller channels terminating within the ductile nodules. In contrast, when scrambled polarization was used, the resulting groove geometries in the three materials were markedly more regular. This is specially the case for cast iron, where the groove's geometry was very straight with minimal branching (see Fig. 3f).

For each of the 77 deep grooves, the total depth of the grooves (L1), envelope opening of the grooves (L2), and the groove depth without branches (L3) were obtained using the methodology detailed in Section 2.4, with a comprehensive summary of all findings presented in Appendix Fig. A.12. To exemplify the effect of laser polarization on the shape of the grooves, 8 out of the 14 groups of deep grooves listed in Table 1 were selected, and their measurements are illustrated in Fig. 4. Fig. 4a reveals that the groove depth (L1) maintains an approximately linear relationship with the logarithm of the laser passes. Similar conclusions can be found in the work by Borowiec et al. [30],

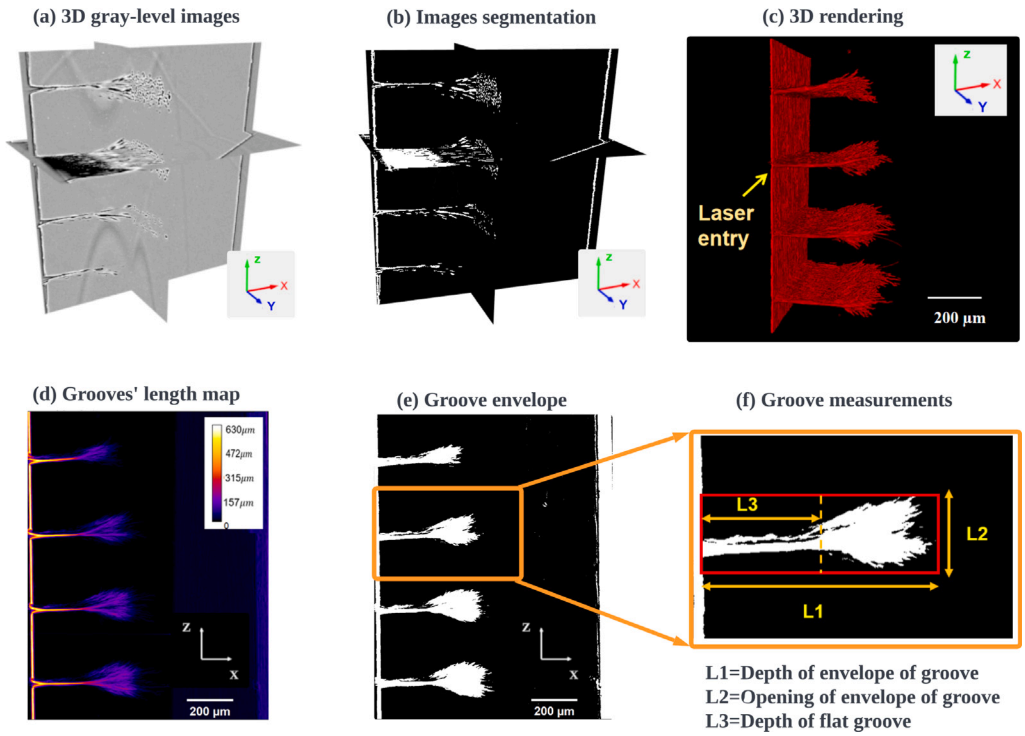

Fig. 2. Schematic representation of the 3D characterization process for grooves within an aluminum sample: (a) 3D gray-level images obtained by SRCT (voxel size 1.3 µm); (b) 2D binary image segmented using the ISODATA algorithm in Fiji software; (c) 3D rendering of the grooves; (d) Y-projection map of the grooves, with varying colors denoting the groove length at different points; (e) Groove envelope projection map, derived by implementing a 10 µm threshold on the Y-projection map in (d); (f) Dimensional measurements of the grooves. This process is the same for synchrotron or laboratory X-rays.

particularly when the depth of the groove exceeds 20 µm. Under identical laser parameters, the deepest grooves are obtained for Ti, followed by cast iron, with Al providing the shallowest grooves. When subjected to the same number of laser passes and for a given entrance length, scrambled polarization usually results in deeper grooves compared to those fabricated with linear polarization across all three materials. This is likely attributable to the laser energy being lost during branching when using linear polarization, while that energy is available to create deeper grooves when using scrambled polarization.

The envelope opening of grooves (L2) (Fig. 4b) created using scrambled polarization is notably smaller compared to those produced with linear polarization. Furthermore, for grooves machined using scrambled polarization, the opening of the grooves does not vary significantly with increasing number of laser passes. Under scrambled polarization, grooves in cast iron exhibit the smallest L2, followed by Al and Ti. In contrast, grooves machined with linear polarization in cast iron have a large L2, which increases as the number of laser passes increases, probably due to the presence of the graphite nodules that accentuate beam divergence and thus branching effects.

Fig. 4c shows that the L3 parameter remain almost constant with increasing laser passes, except for the grooves created using scrambled polarization in cast iron and Ti. Grooves tend to start diverging at a set depth for a given laser power, polarization, and entrance length within the material, as soon as the number of pulses is large enough. Scrambled polarization can significantly increase the depth at which this divergence is observed. In the case of cast iron and Ti, grooves machined with scrambled polarization do not show divergence, resulting in their L1 and L3 being equal and thus increasing with the number or laser passes. However, for aluminum (Al), despite the application of scrambled polarization, deep grooves exhibit some slight divergence beyond a specific depth, resulting in a fairly constant L3 with increasing number of laser passes.

3.2. Effect of laser power on groove shape

To illustrate the effect of laser power on the grooves morphology, deep grooves were machined in titanium (Ti) using laser powers of 1 W and 3 W under the same linear polarization and entrance length (500 µm). Fig. 5 shows that an increase in laser power increases the groove's depth (L1). However, this increase in laser power also leads to a substantial rise in L2, indicating a more pronounced divergence (i.e. branching), as depicted in Fig. 5b.

The evolution of L1 (and L2) with increasing laser passes follow a similar trend at both laser powers. This is however not the case for L3. Fig. 5c reveals that at a low number of laser passes (5), the impact of laser power on L3 is negligible. As the number of laser passes increases, L3 remains constant at low power (1 W) but increases for grooves created with higher power (3 W) up to 15 passes, after which L3 remains constant. In essence, while higher laser power boosts processing efficiency (groove depth), it concurrently compromises processing precision (branching), as illustrated in Fig. 5d. This balance between efficiency and accuracy is crucial in optimizing laser machining processes.

3.3. Effect of groove length on grooves shape

To illustrate the effect of groove length on the morphology of the grooves, deep grooves machined in titanium (Ti) using groove length of 100 µm and 500 µm were analyzed under constant laser power (3 W). For grooves machined with scrambled polarization (green lines in Fig. 6a), longer grooves are deeper at all number of laser passes. This effect can be attributed to more efficient debris removal resulting from the larger processing space in deep grooves with longer entrance lengths, which enhances processing efficiency. In addition, the timing of shutter opening and closing may also have an effect on shorter entrance grooves, as discussed in Section 4.6. However, for grooves created with linear polarization (orange lines in Fig. 6a), a longer groove length correlates

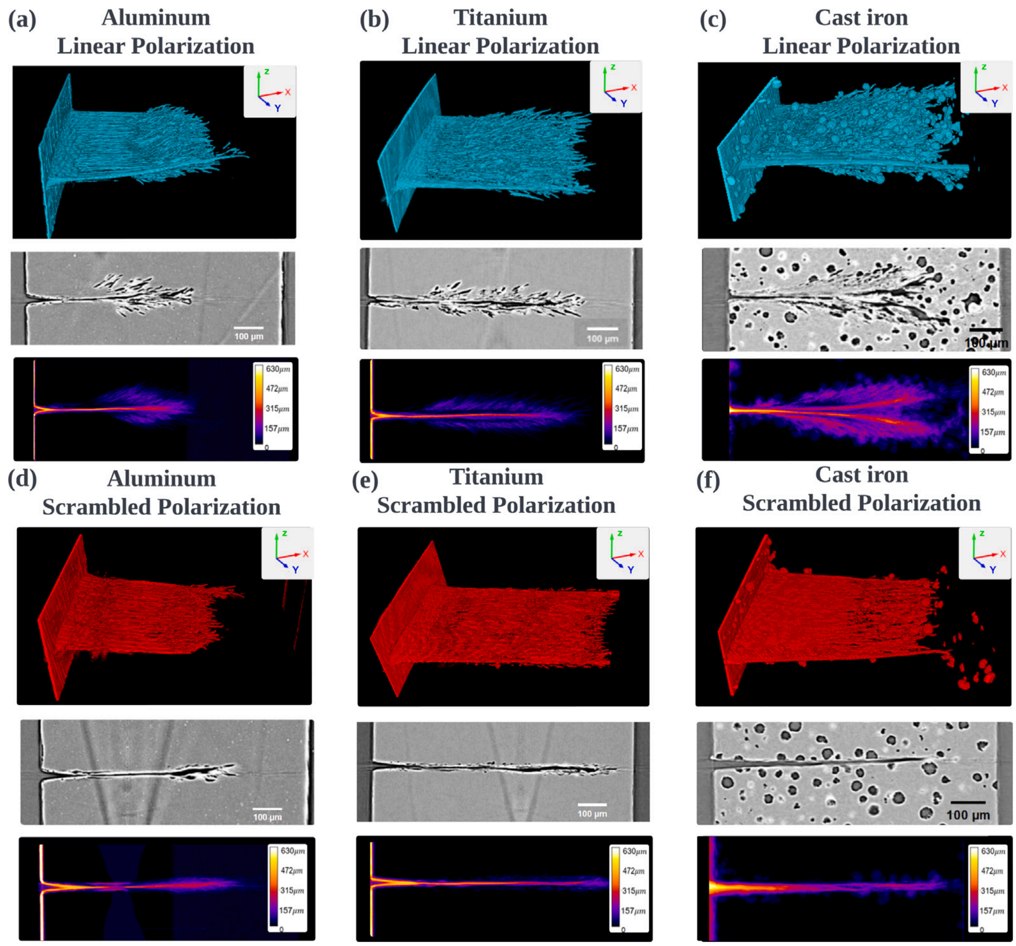

Fig. 3. 3D rendering (top), perpendicular slice taken at the center (containing rotation axis) (middle), and length map of deep grooves (bottom) machined in Al (a), Ti (b) and cast iron (c) using linear polarization and in Al (d), Ti (e) and cast iron (f) using scrambled polarization. The laser power is 3 W, the entrance length is (500 µm), and 80 laser passes are used.

with a deeper machining depth only until the number of laser passes reaches 40. Beyond this point, a shorter groove length yields deeper grooves, potentially due to reduced branching and consequently, less laser energy lost in creating branches and more energy available for deeper machining, as will be explained below.

Fig. 6b illustrates that grooves with 100 µm lengths exhibit significantly smaller L2 values compared to those with 500 µm lengths, a trend more pronounced under linear polarization (with 3D renderings provided in Fig. 6d). As shown in Fig. 6c, under linear polarization, shorter entrance lengths lead to larger divergence (or branching) depths (L3). The impact of laser entrance length can be linked to the flat zone (i.e. without branches), approximately 30-50 µm wide, found on either side of the groove (marked in Fig. 6d by the white arrows). As a result, for grooves machined under linear polarization, the length L3 is greater for the 100 µm entrance width than for the 500 µm entrance width. Additionally, diffraction effects at the sharp edges of the shutter lead to increased laser intensity at the edges of the deep groove [47,48], resulting in deeper features in these areas (as shown in Fig. 6d). Although short shutter opening and closing times ($\leq$ 6.5 ms) were utilized in this study to mitigate this effect, they were insufficient to eliminate it completely. On the other hand, in the case of grooves created with scrambled polarization, the value of L3 equals that of L1 as no obvious branches could be found around the grooves, as seen in Fig. 6e. Due to more efficient debris removal and the effect of shutter opening and closing times during laser processing, the longer entrance lengths result in larger L1 (L3) values.

3.4. Effect of laser machining direction (parallel vs. perpendicular) on groove shapes

Up to this point, the grooves were machined in the direction of the laser polarization, i.e. the laser polarization was parallel to the grooves, a configuration we call here “parallel grooves”. In this section the grooves are perpendicular to the laser polarization; a configuration called “perpendicular grooves”. The imaging results of the grooves with different orientations are shown in Fig. 7. Despite using identical laser parameters (groove entrance length at 100 µm, linear polarization, and laser power at 3 W) and the groove depths being similar for both orientations, their morphological features differ markedly. For parallel grooves, branches form along the groove opening direction (z-axis), whereas for perpendicular grooves, these branches developed along the groove length direction (still on the z-axis). This phenomenon is a result of the laser polarization being fixed along the y-axis, causing the branches to form perpendicular to the polarization direction, i.e., along the z-axis. Section 4.2 offers a discussion of this observation.

4. Discussion

4.1. Benefits of X-ray tomography for observing laser machined grooves

In this study, X-ray tomography was employed to explore the influence of laser parameters on the machining of deep grooves in metals, offering significant advantages over traditional 2D characterizations conducted with microscopes. First, this technique eliminates the need

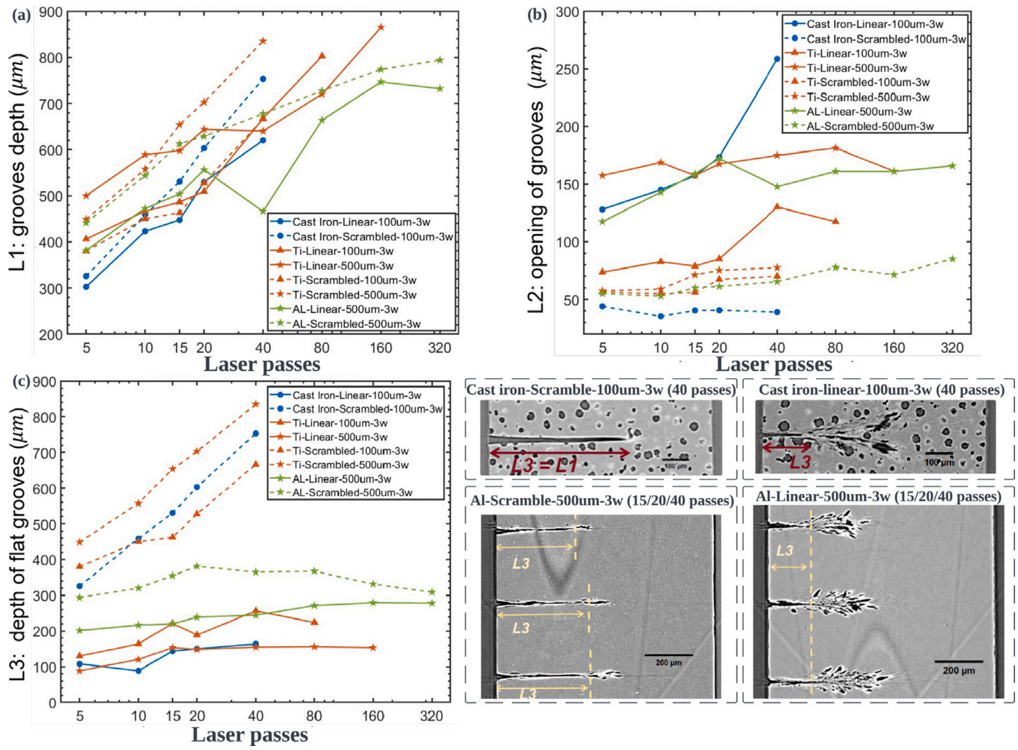

Fig. 4. Effect of laser polarization on groove depth L1 (a), groove opening L2 (b), and depth of flat groove region L3 (c) (with two tomography slices of cast iron and Al).

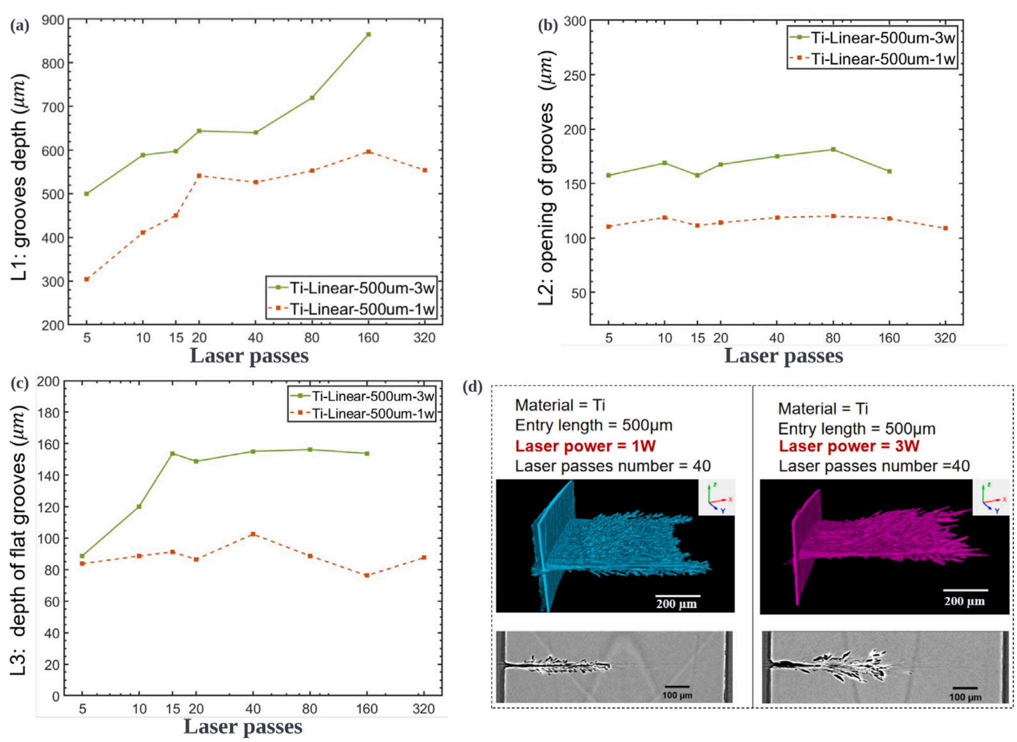

Fig. 5. Effect of laser power on groove depth L1 (a), groove opening L2 (b), and depth of flat groove region L3 (c); (d) 3D renderings and view of the central vertical slice (containing the rotation axis) of deep grooves machined in Ti using laser powers of 1 W and 3 W under linear laser polarization, an entrance length of (500 μm), and 40 laser passes.

for sample cutting and polishing, which is particularly beneficial for metals with low hardness and high ductility, such as aluminum. In such materials, mechanical polishing can lead to the refilling of fine pores, hindering accurate quantitative characterization [49]. X-ray tomography enables three-dimensional characterization and quantitative analysis of deep grooves, providing a more intuitive understanding of their morphology. For example, Nolte [20] analyzed the effect of laser parameters on deep hole manufacturing by comparing the morphology at the entrance and exit holes using a scanning electron microscope (SEM). In Fig. 8, we compare in a similar manner the morphology of

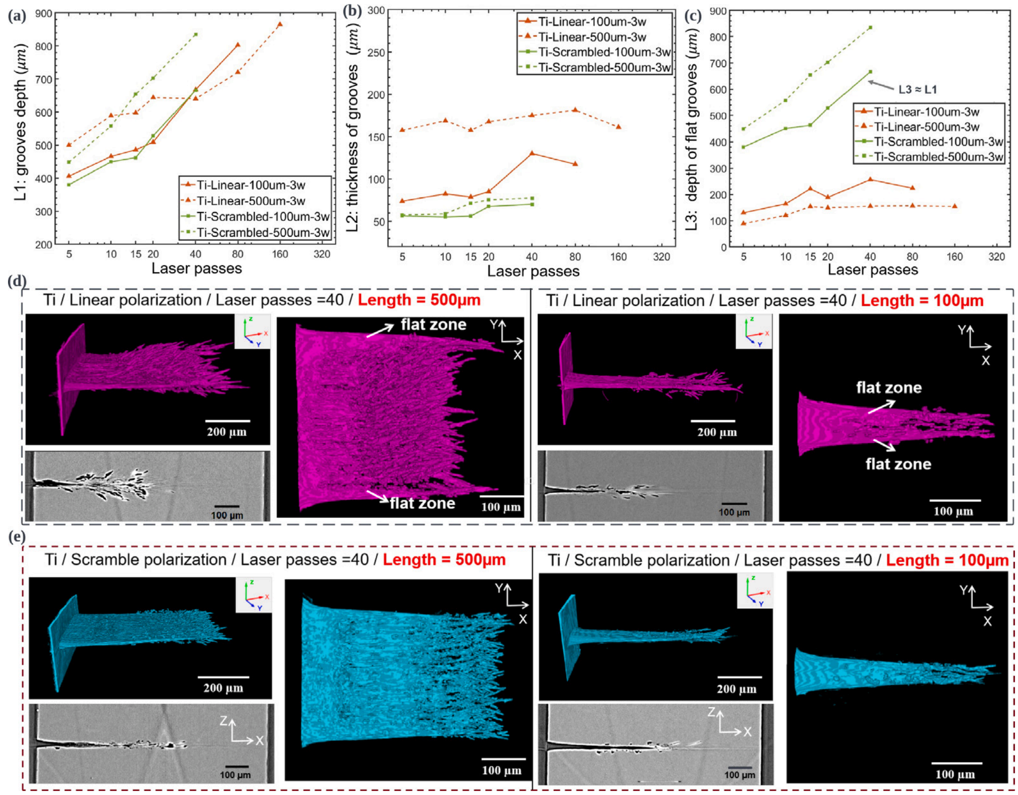

Fig. 6. Effect of groove length (100 μm and 500 μm) under both linear polarization and scrambled polarization on groove depth L1 (a), groove opening L2 (b), and depth of flat groove region L3 (c); (d) 3D renderings and central 2D slices of deep grooves machined in Ti with two different groove lengths (100 μm and 500 μm) under linear polarization; (e) 3D renderings and central 2D slice of deep grooves machined in Ti with two different groove lengths (100 μm and 500 μm) under scrambled polarization.

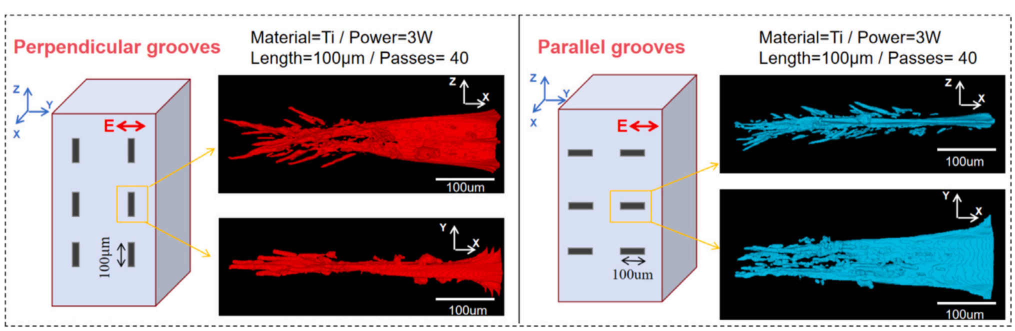

Fig. 7. 3D rendering of deep grooves machined in Ti in two different directions using linear laser polarization, an entrance length of (100 μm), a laser power of 3 W, and 40 laser passes. Left: The grooves are perpendicular to the direction of the laser polarization (called perpendicular groove); Right: The grooves are parallel to the direction of the laser polarization (called parallel groove). The double red arrow indicate the laser polarization direction. (For interpretation of the references to color in this figure legend, the reader is referred to the web version of this article.)

the groove entrance and exit (number of laser passes of 160 and 320) in cast iron and titanium. The results show that for cast iron, machining accuracy of deep grooves can clearly be improved using scrambled polarization. For titanium, grooves created using linear polarization are somewhat shallower and do not go through the sample fully but a similar effect is observed. While the advantage of scrambled v.s. linear polarization is clearly visible in Fig. 8, it is not possible to infer the details of the internal machining process based on these 2D visualizations. On the contrary a 3D image of the groove geometry inside the material (see for example Fig. 2) can provide a more in-depth understanding of the laser matter interactions in the groove and ultimately offer the possibility to determine optimal machining conditions.

The quality of the images produced by this technique is influenced by factors such as the type of X-ray source, pixel size, and several other parameters (see [50] for a list). The effect of the type of X-ray source is illustrated in Fig. 9, which shows 3D images of grooves in titanium under linear polarization with a laser power of 3 W, a length of 500 μm, and 5 and 10 laser passes. Synchrotron Radiation Computed

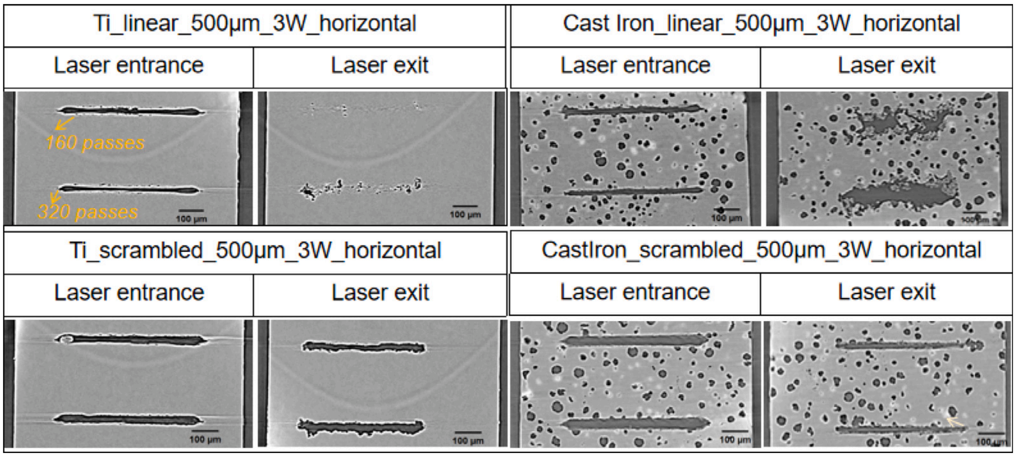

Fig. 8. Comparison of the entrance and exit morphology of grooves in Ti and Cast Iron (Laser Power: 3 W, Length: 500 μm, Laser Passes: 160 and 320, Linear/Scrambled Polarization). All images are vertical slices from SRCT at the entrance and exit of the laser, respectively.

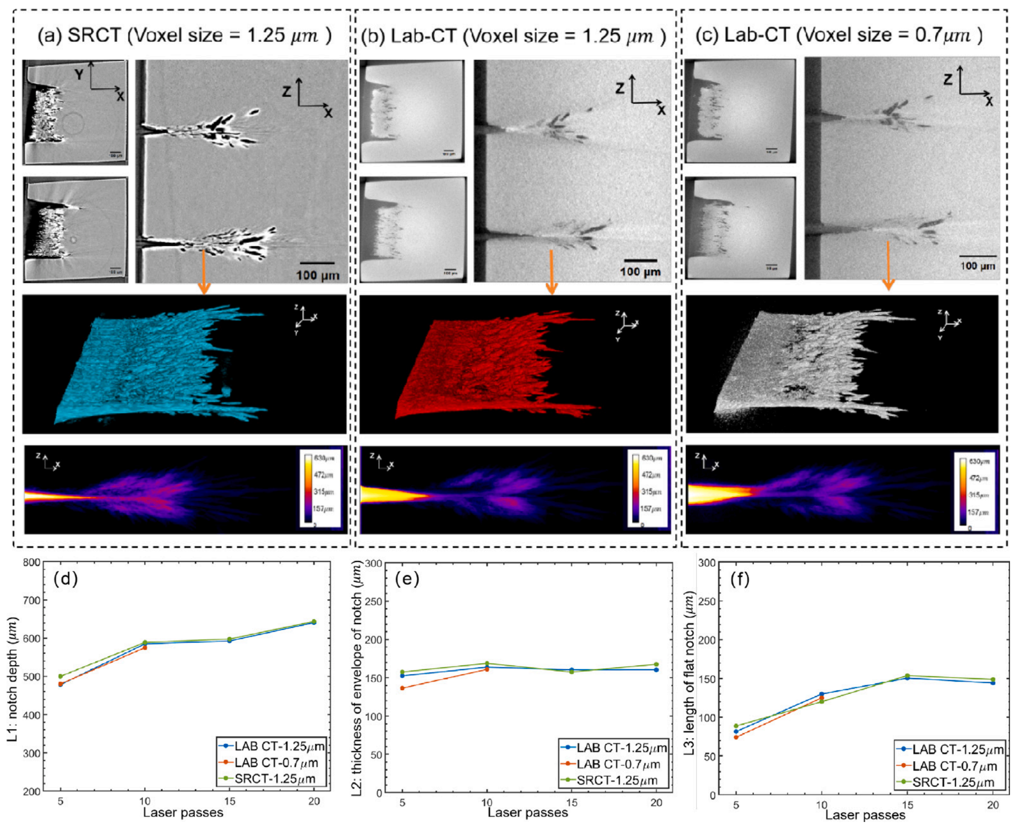

Fig. 9. SRCT and Lab-CT 3D imaging and measurements of microgrooves in titanium (Ti) under linear polarization with a laser power of 3 W, a length of 500 μm, and 5 and 10 laser passes. (a) 3d imaging results by SRCT (voxel size 1.25 μm); (b) 3d imaging results by Lab-CT (voxel size 1.25 μm); (c) 3d imaging results by Lab-CT (voxel size 0.7 μm); (d) groove depth L1, (e) groove opening L2, (f) and depth of flat groove region L3.

Tomography (SRCT) images were obtained with a voxel size of 1.25 μm and laboratory tomography images (Lab-CT) with voxel sizes of 1.25 μm and 0.7 μm.

As shown in Fig. 9a, b, and c, SRCT shows a superior ability to detect minute features compared to Lab-CT, primarily due to the phase contrast provided by the highly coherent X-ray beam [50]. However, SRCT images exhibit Fresnel fringes around the grooves, which can complicate the precise segmentation of fine features. To address this, reconstruction methods based on phase retrieval, such as the Paganin method [51], have been employed to generate images with “phase-only” contrast. Nonetheless, this method can sometimes lead to image blurring, reducing the recognizability of fine details.

Fig. 9d, e, and f illustrate that the measurements for L1, L2, and L3 parameters derived from both SRCT and Lab-CT (with two different voxel sizes) are closely aligned, confirming that Lab-CT is also capable of macroscopically characterizing deep grooves in 3D. One important drawback of Lab-CT however is that it requires relatively long imaging times. For example, the scanning duration for a single SRCT scan in this study is approximately 3 min, significantly faster than the 60-minute scan time required for Lab-CT at a comparable resolution. In spite of this, given that Lab-CT is more accessible and less expensive, it presents a compelling option for future morphological characterization of deep grooves.

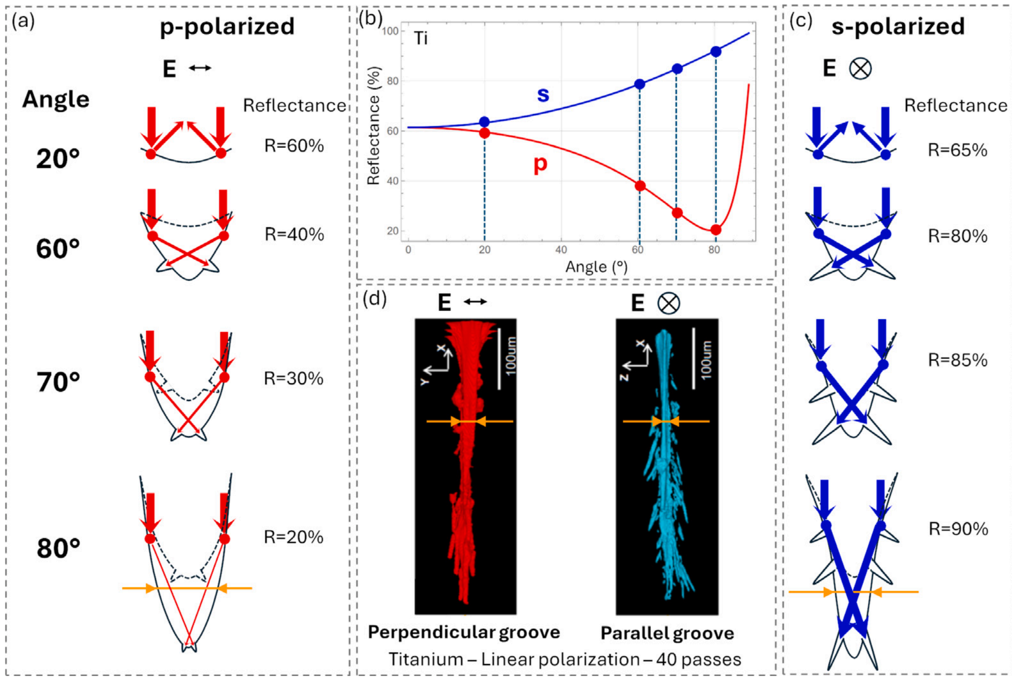

Fig. 10. Mechanistic picture of groove and branching formation under p-polarized and s-polarized irradiation: (a) Morphological evolution of deep grooves under p-polarized irradiation. (b) Reflectance curves as a function of laser incidence angle under p-polarized and s-polarized irradiation for titanium. (c) Morphological evolution of deep grooves under s-polarized irradiation. (d) 3D rendering of deep grooves machined in Ti with p-polarized irradiation, an entrance length of (100 μm, a laser power of 3 W, and 40 laser passes); (e) 3D rendering of deep grooves machined in Ti with s-polarized irradiation with an entrance length of (100 μm), a laser power of 3 W, and 40 laser passes.

4.2. Groove formation and limited branching under fixed p-polarized light — perpendicular grooves

Fig. 10 presents a mechanistic picture for the formation of lateral branches during machining of deep grooves in metals as reported here. The first important parameter that needs to be considered is the polarization- and angle-dependent laser beam reflections off the groove wall. Fig. 10b shows that the percent reflectance off a surface depends on both the incoming light polarization (s-polarized or p-polarized) and on the angle the incoming light makes with the normal to that surface. P-polarized light has an electric field polarized parallel to the plane of incidence (i.e. the plane that contains the incident laser beam and the normal to the surface), while s-polarized light is perpendicular to this plane. S-polarized light (blue curve in Fig. 10b) sees an increase in reflectance with increasing angle while p-polarized light (red curve in Fig. 10b) show a significant decrease of reflectance with angle up to an angle of about 80° at which point the reflectance increases sharply again. Note that Fig. 10b was generated using Fresnel equations [52] for titanium at a laser wavelength of 1030 nm and with the real and imaginary parts (extinction coefficient) n=3.416 and κ =3.992 of the index of refraction for titanium. The absolute values seen in Fig. 10b will change for the different materials studied here, but the general trend is maintained between s- and p-polarized light.

Fig. 10a presents a mechanistic picture for the laser drilling process of a groove with p-polarized light (perpendicular grooves). The laser beam has a Gaussian intensity profile which results in more material ablation at the center of the groove compared to its edges. As the groove becomes deeper with increasing laser pulses, the walls of the groove become steeper and the angle between the incoming laser beam and the normal to the wall increases (from 20° to 80° in Fig. 10a). As the angle increases, the p-polarized light is more absorbed and thus less reflected (as per red curve in Fig. 10b). If a reflection of 40% could produce some branching at 60°, it will produce less (or shallower) branching at 80° where the reflection is only 20%. Furthermore, less energy reflected means more energy absorbed by the material when the laser first hits the groove wall, which means more ablation and removal of previously created structures (i.e. branches created from previous laser pulses can be removed by subsequent pulses). In conclusion, as the groove becomes deeper, less reflected energy is available to form branches and more energy is directly absorbed by the groove wall first hit by the laser, resulting in relatively thick grooves as shown by the double orange arrow in the schematic and confirmed by the 3D rendering of a groove in Fig. 10d. It should be noted that the reflectance of p-polarized light increases sharply going from 80° to 90° and thus one would expect some branching once the walls of the grooves are very steep, which take place when the groove is very deep. This could explain the presence of some branches at the bottom of the groove in Fig. 10d.

4.3. Groove formation and extensive branching under fixed s-polarized light — parallel grooves

Fig. 10c presents a mechanistic picture for the laser drilling process of a groove with s-polarized light (parallel grooves). Contrary to p-polarized light, s-polarized light in increasingly reflected as the groove wall becomes deeper and thus steeper (blue curve in Fig. 10b), which results in deeper branches with increasing groove depth as shown in the schematic in Fig. 10c. It should be noted that the formation of the branches comes from the accumulation of many pulses. Furthermore, unlike p-polarized light, less energy is available for ablation when the laser first hits the groove wall (as more is reflected), which means that branches are not removed as the groove deepens and that the groove can remain fairly thin (as shown by the double orange arrow in Fig. 8e and confirmed by the SRCT reconstruction of a groove in Fig. 10e.

4.4. Effect of power on groove depth and branching

The mechanistic picture described in Fig. 10 can also explain the effect of laser power on groove depth and the extent of branching seen in Section 3.2. As more power is used (3 W vs 1 W), not only is more power available for machining deeper and wider grooves (Fig. 5a) but also more power is reflected on the groove wall and available to machine deeper branches as seen in Fig. 5b.

4.5. Start of branching — parameter L3

The 3D images of the machined grooves clearly show a minimum depth over which the groove is smooth and after which branching starts (distance L3 defined in Fig. 2f). This minimum depth can be explained by the wall angle which needs to be steep enough to reflect light sufficiently to create branches. As explained in Fig. 10, when the wall angle is small (e.g 20°), the laser beam is reflected outside the groove. As the groove deepens, the laser light starts to be reflected on the opposite wall (e.g 60°). However, while light can now be reflected on the opposite wall, its energy might not be large enough to create deep branches. As the groove deepens, the amount of reflected light increases sufficiently (under s-polarization) to obtain deep grooves. The depth at which branches start forming (L3) depends on the ablation threshold of the material and is thus material dependent (see Fig. 4c).

4.6. Note on the effect of laser shutter opening on groove morphology

It should be noted that the laser shutter opening and closing times are 4.3 ms and 6.5 ms respectively. At a laser scanning speed of 10 mm/s, the distances traveled by the laser beam during shutter opening and closing are 43 μm and 65 μm respectively. This means that for the short grooves, the shutter cannot fully open before it needs to close again. In addition to the easier debris removal associated with grooves that have longer entrances (500 μm), the fact that grooves with 100 μm entrances are not exposed to the full laser power due to shutter opening and closing times may also explain why longer grooves are deeper than shorter ones (see Fig. 6a). The same reasoning can explain the depth of the branches, which is smaller for the 100 μm grooves as less energy is available.

4.7. Groove formation under scrambled linearly polarized light (i.e. rotating polarization or polarization trepanning)

Linear polarization (s-polarized in particular) creates deep branches as a result of many pulses reflecting from the groove surface and hitting the opposite wall of the groove. Scrambled polarization sees many linearly polarized pulses hitting the sample at different polarization angles (See Fig. 1), resulting in fewer and shallower branches. Indeed, branching is not only due to light reflection from the groove wall but also from the accumulation of many pulses at a given polarization. If the polarization angle changes between pulses, the start of the branching process created by one pulse will be erased by the next, coming at a different polarization angle, resulting in a clean grooves without branching (see Fig. 2f).

Grooves created with scrambled polarization also tend to have greater depths as the energy is not lost in creating the branches until much later in the machining process. This effect is clearly observed for long parallel grooves (500 μm deep) in Fig. 4a) and less pronounced for shorter grooves (100 μm deep). Short perpendicular grooves (100 μm) initially have a similar L1 compared to parallel and scrambled (Fig. 11a) but are deeper (higher L1) after about 15 passes. This increase in length is probably due to the significant branching in the x–z plane as shown in Fig. 11f where a few branches can extend over a relatively long distance, resulting in large L1 values.

In terms of groove opening and extent of branching evaluated by L2 (Fig. 11b), the opening of the parallel grooves is the largest,[1] while perpendicular and scrambled have low opening. This result is consistent with limited branching in the x–y plane for perpendicular grooves and limited or suppressed branching when using scrambled polarization as explained above.

The effects of groove orientation and polarization are also clearly visible in the L3 parameter (groove depth before significant branching occurs) in Fig. 11c. For parallel grooves under linear polarization, branching appears early because more energy is reflected on the wall (as per Fig. 10c) while for perpendicular grooves, branching takes place only when the groove is very deep and the sidewalls are steep enough, when the angle is close to 90° and the reflections increase sharply (see Fig. 10b). Scrambled polarization has the longest L3 because branching is prevented altogether.

5. Conclusion

X-ray tomography was used to quantitatively characterize in three-dimensions the effect of laser parameters on the morphology of deep laser-machined grooves in metals. The findings underscore the critical role of laser polarization in dictating groove shape. Specifically, when the polarization is aligned with (i.e. parallel to) the groove, a proliferation of branches form on both sides of the groove beyond a certain depth. The extent of branching increases with increasing laser power and groove entrance length, and is material dependent (e.g. more branching in cast iron). Scrambled polarization markedly diminishes the occurrence of branching, thereby augmenting the precision of the laser machining process. Through a comparative analysis of deep grooves created using different polarization scenarios, we have substantiated a mechanistic picture where branching and groove geometry originate from angle-dependent reflections of the laser beam on the groove walls. This study also demonstrates the benefits of X-ray tomography for the characterization of deep laser machined features.

CRediT authorship contribution statement

Ce Xiao: Writing – review & editing, Writing – original draft, Visualization, Validation, Methodology, Investigation, Conceptualization. **Jean-Yves Buffiere:** Writing – review & editing, Methodology, Funding acquisition, Conceptualization. **Arnaud Weck:** Writing – review & editing, Writing – original draft, Visualization, Validation, Methodology, Investigation, Conceptualization.

Declaration of competing interest

The authors declare that they have no known competing financial interests or personal relationships that could have appeared to influence the work reported in this paper.

Acknowledgments

We acknowledge the European Synchrotron Radiation Facility, Grenoble, France for provision of synchrotron radiation beamtime at beamline ID11 (Number: ME-1559). The Natural Sciences and Engineering Research Council of Canada (NSERC) is also acknowledged. The authors thank specifically M. Wolfgang Ludwig for their help with the successful synchrotron experiments.

Appendix

The envelope length (L1), opening (L2), and length of the flat region (L3) were measured for each of the 77 notches using the method presented in Section 2.4, and the results are shown in Fig. A.12.

[1] The measurements for the perpendicular groove in Fig. 11 were extracted in the x–y plane instead of the x–z plane for parallel grooves.

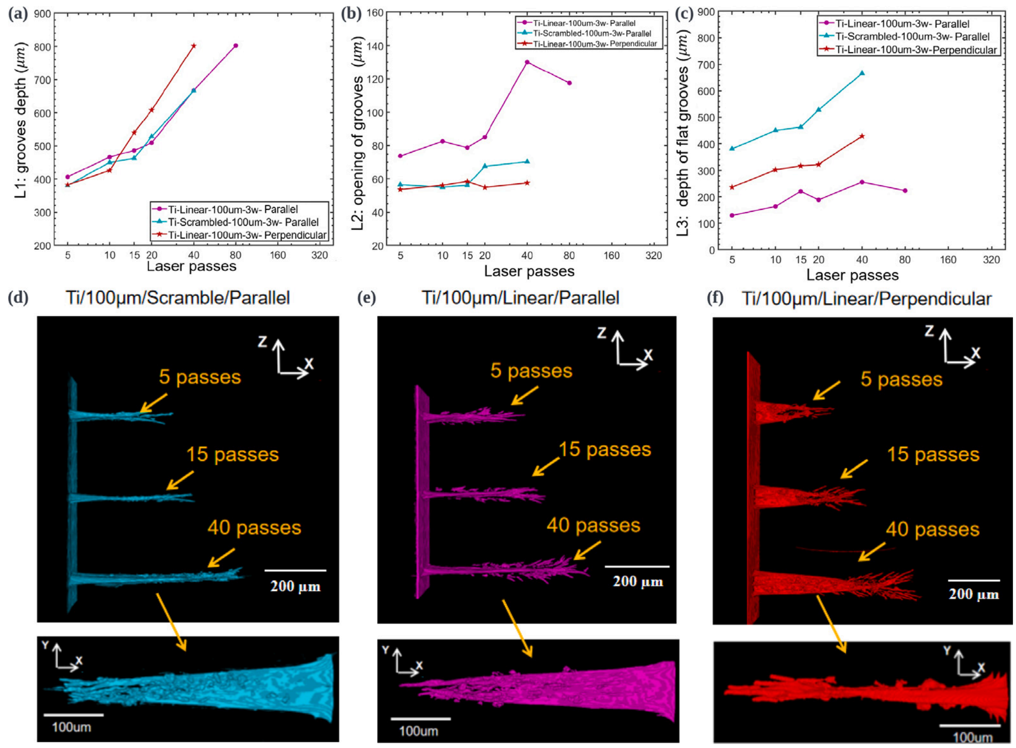

Fig. 11. Effect of laser machining direction on groove depth L1 (a), groove opening L2 (b), and depth of flat groove region L3 (c); (d) 3D renderings of parallel grooves machined inside Ti with a groove length of 100 μm under scrambled polarization; (e) 3D renderings of parallel deep grooves machined inside Ti with a groove length of 100 μm under linear polarization (s-polarized); (f) 3D renderings of perpendicular deep grooves machined inside Ti with a groove length of 100 μm under scrambled polarization (p-polarized).

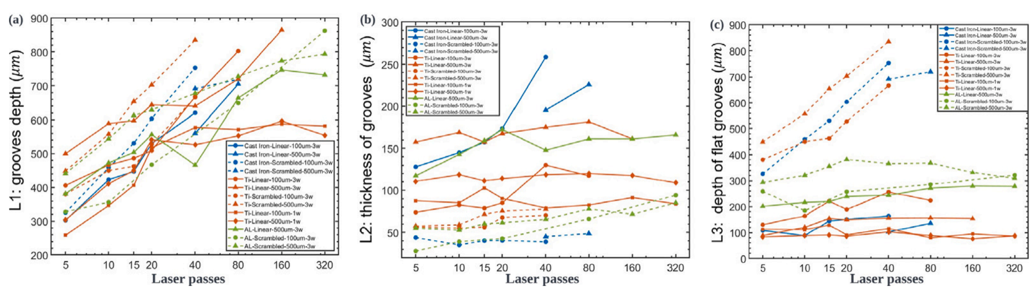

Fig. A.12. Measurements of all the 77 notches fabricated with different laser parameters in the 3 different metals (Cast iron/Al/Ti): groove depth L1 (a), groove opening L2 (b), and depth of flat groove region L3 (c).

References

[1] Malinauskas M, Žukauskas A, Hasegawa S, Hayasaki Y, Mizeikis V, Buividas R, et al. Ultrafast laser processing of materials: from science to industry. Light: Sci Appl 2016;5(8):e16133.

[2] Ahmmed KMT, Grambow C, Kietzig AM. Fabrication of micro/nano structures on metals by femtosecond laser micromachining. Micromachines 2014;5(4):1219–53.

[3] Vorobyev AY, Makin VS, Guo C. Periodic ordering of random surface nanostructures induced by femtosecond laser pulses on metals. J Appl Phys 2007;101(3):034903.

[4] Mannion PT, Magee J, Coyne E, O'Connor GM, Glynn TJ. The effect of damage accumulation behaviour on ablation thresholds and damage morphology in ultrafast laser micro-machining of common metals in air. Appl Surf Sci 2004;233(1):275–87.

[5] Xu S, Chen Y, Liu H, Miao X, Yuan X, Jiang X. Femtosecond laser ablation of Ti alloy and Al alloy. Optik 2020-06-01;212:164628.

[6] Her TH, Finlay RJ, Wu C, Deliwala S, Mazur E. Microstructuring of silicon with femtosecond laser pulses. Appl Phys Lett 1998;73(12):1673–5.

[7] Nayak BK, Gupta MC, Kolasinski KW. Spontaneous formation of nanospiked microstructures in germanium by femtosecond laser irradiation. Nanotechnology 2007;18(19):195302.

[8] Choudhury IA, Shirley S. Laser cutting of polymeric materials: An experimental investigation. Opt Laser Technol 2024;42(3):503–8.

[9] Stepak B, Grudzien N, Kowalska K, Stepanenko Y, Nejbauer M. High-speed cleaving of glass and polymers using ultrafast fiber laser. J Laser Appl 2022;35(1):012005.

[10] Zhang Y, Lowe RM, Harvey E, Hannaford P, Endo A. High aspect-ratio micromachining of polymers with an ultrafast laser. Appl Surf Sci 2002;186(1):345–51.

[11] Perrie W, Rushton A, Gill M, Fox P, O'Neill W. Femtosecond laser micro-structuring of alumina ceramic. Appl Surf Sci 2005;248(1):213–7.

[12] Ihlemann J, Scholl A, Schmidt H, Wolff-Rottke B. Nanosecond and femtosecond excimer-laser ablation of oxide ceramics. Appl Phys A 1995;60(4):411–7.

[13] Kim SH, Sohn I-B, Jeong S. Ablation characteristics of aluminum oxide and nitride ceramics during femtosecond laser micromachining. Appl Surf Sci 2009;255(24):9717–20.

[14] Nikumb S, Chen Q, Li C, Reshef H, Zheng HY, Qiu H, et al. Precision glass machining, drilling and profile cutting by short pulse lasers. In: ICMAT 03, Thin Solid Films In: ICMAT 03, 2024;477(1).216–21,

[15] Sipe JE, Young JF, Preston JS, van Driel HM. Laser-induced periodic surface structure. I. Theory. Phys Rev B 1983;27(2):1141–54.

[16] Bonse J, Krüger J, Höhm S, Rosenfeld A. Femtosecond laser-induced periodic surface structures. J Laser Appl 2012;24(4):042006.

[17] Bonse J, Kirner SV, Krüger J. Laser-induced periodic surface structures (LIPSS). In: Sugioka K, editor. Handbook of laser micro- and nano-engineering. Springer International Publishing; 2020, p. 1–59.

[18] Young JF, Preston JS, van Driel HM, Sipe JE. Laser-induced periodic surface structure. II. Experiments on Ge, Si, Al, and brass. Phys Rev B 1983;27(2):1155–72.

[19] Xia B, Jiang L, Li X, Yan X, Lu Y. Mechanism and elimination of bending effect in femtosecond laser deep-hole drilling. Opt Express 2015;23(21):27853–64.

[20] Nolte S, Momma C, Kamlage G, Ostendorf A, Fallnich C, von Alvensleben F, et al. Polarization effects in ultrashort-pulse laser drilling. Appl Phys A 1999-05-01;68(5):563–7.

[21] Kononenko T, Konov V, Garnov S, Klimentov S, Dausinger F. Dynamics of deep short pulse laser drilling: ablative stages and light propagation. Laser Phys-Lawrence 2001;11(3):343–51.

[22] Tao S, Wu B, Lei S. Study of laser beam propagation in microholes and the effect on femtosecond laser micromachining. J Appl Phys 2011;109(12).

[23] Jiao L, Ng E, Zheng H, Zhang Y. Theoretical study of pre-formed hole geometries on femtosecond pulse energy distribution in laser drilling. Opt Express 2015;23(4):4927–34.

[24] Shah L, Tawney J, Richardson M, Richardson K. Self-focusing during femtosecond micromachining of silicate glasses. IEEE J Quantum Electron 2004;40(1):57–68.

[25] Döring S, Szilagyi J, Richter S, Zimmermann F, Richardson M, Tünnermann A, et al. Evolution of hole shape and size during short and ultrashort pulse laser deep drilling. Opt Express 2012;20(24):27147–54.

[26] Niziev VG, Nesterov AV. Influence of beam polarization on laser cutting efficiency. J Phys D: Appl Phys 1999;32(13):1455.

[27] Wang R, Dong X, Wang K, Sun X, Fan Z, Duan W, et al. Polarization effect on hole evolution and periodic microstructures in femtosecond laser drilling of thermal barrier coated superalloys. Appl Surf Sci 2021-01-30;537:148001.

[28] A Z, Zou G, Yu H, Feng B, Du C, Liu L. Polarization-dependent, beam reflection-regulated hole shaping dynamics visualized by in-situ imaging of ultrafast laser drilling process. Precis Eng 2024-03-01;86:153–9.

[29] Chen Y, Cao Y, Wang Y, Zhang L, Shao G, Zi J. Fabrication of grooves on polymer-derived SiAlCN ceramics using femtosecond laser pulses. Ceram Int 2020;46(8, Part B):11747–61.

[30] Borowiec A, Haugen H. Femtosecond laser micromachining of grooves in indium phosphide. Appl Phys A 2004-08-01;79(3):521–9.

[31] Chen T, Pan A, Li C, Si J, Hou X. Study on morphology of high-aspect-ratio grooves fabricated by using femtosecond laser irradiation and wet etching. Appl Surf Sci 2015-01-15;325:145–50.

[32] Bärsch N, Körber K, Ostendorf A, Tönshoff K. Ablation and cutting of planar silicon devices using femtosecond laser pulses. Appl Phys A 2003;77(2):237–42.

[33] Wang XC, Zheng HY, Chu PL, Tan JL, Teh KM, Liu T, et al. High quality femtosecond laser cutting of alumina substrates. Opt Lasers Eng 2010;48(6):657–63.

[34] Wei J, Ye Y, Sun Z, Liu L, Zou G. Control of the kerf size and microstructure in inconel 738 superalloy by femtosecond laser beam cutting. Appl Surf Sci 2016;370:364–72.

[35] Shanjin L, Yang W. An investigation of pulsed laser cutting of titanium alloy sheet. Opt Lasers Eng 2006;44(10):1067–77.

[36] Junet A, Messager A, Weck A, Nadot Y, Boulnat X, Buffiere J-Y. Internal fatigue crack propagation in a Ti-6Al-4V alloy: An in situ study. Int J Fatigue 2023-03-01;107450.

[37] Xiao C, Sun R, Adrien J, Lachambre J, Nadot Y, Weck A, et al. 3D characterization of closure of surface and internal fatigue cracks in nodular cast iron using digital volume correlation of laboratory X-ray tomography images. Int J Fatigue 2024-05-01;182:108226.

[38] Maire E, Withers PJ. Quantitative X-ray tomography. Int Mater Rev 2014;59(1):1–43.

[39] Withers PJ, Bouman C, Carmignato S, Cnudde V, Grimaldi D, Hagen CK, et al. X-ray computed tomography. Nat Rev Methods Primers 2021;1(1):1–21.

[40] Cunningham R, Narra SP, Montgomery C, Beuth J, Rollett AD. Synchrotron-based X-ray microtomography characterization of the effect of processing variables on porosity formation in laser power-bed additive manufacturing of ti-6al-4V. JOM 2017;69(3):479–84.

[41] du Plessis A, Yadroitsev I, Yadroitsava I, Le Roux SG. X-Ray microcomputed tomography in additive manufacturing: A review of the current technology and applications. 3D Print Addit Manuf 2018;5(3):227–47.

[42] Naragani DP, Shade PA, Kenesei P, Sharma H, Sangid MD. X-ray characterization of the micromechanical response ahead of a propagating small fatigue crack in a Ni-based superalloy. Acta Mater 2019;179:342–59.

[43] Nasrollahi V, Penchev P, Jwad T, Dimov S, Kim K, Im C. Drilling of micron-scale high aspect ratio holes with ultra-short pulsed lasers: Critical effects of focusing lenses and fluence on the resulting holes' morphology. Opt Lasers Eng 2018;110:315–22.

[44] Vanwersch P, Schildermans S, Nagarajan B, Van Bael A, Castagne S. Three-dimensional modelling of femtosecond laser ablation of metals. Lasers Manuf Mater Process 2022;9(4):515–31.

[45] Xiao C, Létang JM, Buffiere JY. Characterization of internal fatigue cracks in aluminum alloys by simulation of phase contrast tomography. Sci Rep 2022;12.

[46] Velasco FR. Thresholding using the isodata clustering algorithm. Tech. rep., Maryland Univ College Park Computer Science Center; 1979.

[47] Davidović MD, Davidović MD, Sanz AS, Božić M, Vasiljević D. Trajectory-based interpretation of laser light diffraction by a sharp edge. J Russ Laser Res 2018;39(5):438–47.

[48] Polyanskii PV, Bogatiryova GV. EDW: edge diffraction wave, edge dislocation wave, or whether tertio est datur? The bicentenary of Thomas Young's wave diffraction theory. Sel Pap Fifth Int Conf Correl Opt 2002;4607:109–24.

[49] Buffière JY, Maire E, Cloetens P, Lormand G, Fougères R. Characterization of internal damage in a MMCp using X-ray synchrotron phase contrast microtomography. Acta Mater 1999;47(5):1613–25.

[50] Stock SR. MicroComputed Tomography: Methodology and Applications. 2nd ed.. CRC Press; 2019-12-16.

[51] Paganin D, Mayo SC, Gureyev TE, Miller PR, Wilkins SW. Simultaneous phase and amplitude extraction from a single defocused image of a homogeneous object. J Microsc 2002;206:33–40.

[52] Hecht E. Optics. 5th ed.. 325, Pearson; 2021.